Artigo

Estimation of Soybean Evapotranspiration Using SSEBop Model with High-Resolution Imagery from an Unmanned Aerial Vehicle

Raphael Augusto das Chagas Noqueli Casari[1] (iD), Marina Bilich Neumann[2],
Walter Quadros Ribeiro Junior[3], Diogo Olivetti[1], Cássio Jardim Tavares[5],
Lucas Felisberto Pereira[4], Maria Lucrécia Gerosa Ramos[2], André Ferreira Pereira[3],
Sebastião Pedro da Silva Neto[3], Henrique Llacer Roig[1]

[1]*Laboratório de Geoprocessamento, Programa de Pós-Graduação em Geociências Aplicadas e Geodinâmica, Instituto de Geociências, Universidade de Brasília, Brasília, DF, Brazil.*
[2]*Faculdade de Agronomia e Medicina Veterinária, Universidade de Brasília, Brasília, DF, Brazil.*
[3]*Embrapa Cerrados, Empresa Brasileira de Pesquisa Agropecuária, Planaltina, DF, Brazil.*
[4]*Instituto Federal Goiano, Campus Posse, Posse, GO, Brazil.*
[5]*Instituto Federal Goiano, Campus Cristalina, Cristalina, GO, Brazil.*

Abstract

Evapotranspiration (ET) is one of the most important processes in the hydrologic cycle, constituting the main responsible for water losses at the surface. Several evapotranspiration models use information from surface temperature and vegetation indices captured by remote sensors such as MODIS and LANDSAT to estimate the ETc value. The objective of this study is to apply SSEBop model to estimate ETc of soybean in a field experiment under four water regimes, using high-resolution multispectral and thermal images collected from remotely piloted aircraft (RPA). Surface temperature and NDVI maps were generated as sources for evapotranspiration estimation. From a Python script, spatial variability maps of ETc were generated at different phenological stages of the crop. The quality of the model for ETc estimates was performed by comparing the modeling results with leaf transpiration data measured in the field using an infrared gas analyzer, whose results showed a good correlation ($R^2 = 0.76$). These results demonstrated the possibility of transferring a model originally developed for processing low to medium-resolution satellite images to high-resolution spatial-temporal images acquired by RPA with small adaptations in the original algorithm, generating great potential for new studies on an experimental and field scale.

Keywords: remote sensing, RPA, Glycine max L.

Estimativa da Evapotranspiração da Soja Pelo Modelo SSEBop Utilizando Imagens de Alta Resolução Obtidas Por Aeronave Remotamente Pilotada

Resumo

A evapotranspiração (ET) é um dos mais importantes processos do ciclo hidrológico, constituindo-se o principal responsável pelas perdas de água na superfície. Vários modelos de evapotranspiração utilizam informações da temperatura da superfície e índices de vegetação captadas por sensores remotos tais como o MODIS e a série LANDSAT para estimar o valor de ETc. O objetivo deste estudo aplicar o modelo SSEBop para estimativa da ETc da soja (Glicine max. L) em um campo experimental submetida a quatro regimes hídricos, utilizando imagens multiespectrais e termais de alta resolução coletadas com uso de aeronave remotamente pilotada. Mapas de temperatura da superfície e NDVI foram gerados como fontes para a estimativa da evapotranspiração. A partir de um script em Python, mapas de variabilidade espacial da ETc foram gerados para diferentes estádios fenológicos da cultura. A qualidade do modelo de estimativas de ETc foi realizada comparando-se os resultados da modelagem com os dados transpiração foliar medida no campo através de um analisador de gases por infravermelho, cujos resultados mostraram boa correlação ($R^2 = 0,76$). Estes

---

Corresponding author: Raphael Augusto das Chagas Noqueli Casari. E-mail: casari.raphael@gmail.com.

resultados demostraram a possibilidade de transferência de um modelo originalmente desenvolvido para processamento de imagens de satélite de baixa a média resolução para imagens de alta resolução espaço temporal adquiridos por RPA a partir de pequenas adaptações no algoritmo original, gerando um grande potencial para novos estudos em escala experimental e de campo.

Palavras-chave: sensoriamento remoto, ARP, Glycine max L.

1. Introduction

The use of data from remote sensing has received a significant increase in environmental studies over the last few decades. Gradually, remote sensing techniques have been improved and have become an important and indispensable tool for the assessment and monitoring of natural and human ecosystems (Thorp *et al.*, 2004; Jianya *et al.*, 2008; Franco *et al.*, 2013; Bounouh *et al.*, 2017). In these evaluation processes, images acquired by thermal, multispectral and hyperspectral cameras transported by Remotely Piloted Aircraft (RPA) have been used (Franco *et al.*, 2013).

In the particular case of agriculture, the use of spectral images has improved the evaluation process under controlled conditions, such as water stress conditions, making the monitoring of this process much more efficient and accurate, in addition to being a powerful tool for the evaluation of cultivars already installed in production fields (Sishodia *et al.*, 2020). Over the years, science has revealed different evidence that have contributed to the development of methodologies currently used to estimate real Evapotranspiration (ETa) from data collected by remote sensing. ETa is an important variable of the water balance since it corresponds to more than 50% of the precipitated water (Tucci, 2012). In addition, it is a complex variable to measure, as it presents multiscale variability, both spatial and temporal. In this context, the remote sensing approach has been shown to be efficient in estimating evapotranspiration (Karimi and Bastiaanssen, 2015; Paula *et al.*, 2019; Vale *et al.*, 2022).

According to Allen *et al.* (1998), evapotranspiration is the sum of the evaporation of water contained in the soil surface with the transpiration of plants. In general, ETa models can be categorized into two types: empirical methods and analytical methods. Analytical methods seek to establish the physical processes and require data measured directly and indirectly by remote sensing and surface instruments, while empirical methods establish relationships derived from data obtained by remote sensing with data measured at the surface through statistical models (Allen *et al.*, 2007).

In the analytical approach, the models can be classified as one-layer or two-layer, where the main difference is the separation of the surface energy flow into one or two components, separating the calculation of the physical processes that occur in the soil from those that occur in the vegetation canopy. Although two-layer models are considered an evolution of one-layer models, one-layer models are widely disseminated through different methodologies that have been developed over time, such as Surface Energy Balance for Land - SEBAL (Bastiaanssen *et al.*, 1998), the Mapping Evapotranspiration with Internalized Calibration - METRIC (Allen *et al.*, 2007) and the Surface Energy Balance System - SEBS (Su, 2002), among others.

Another methodology to be mentioned and used in this study is the Simplified Surface Energy Balance Approach - SSEBop, developed by Senay *et al.* (2013). This model determines the actual evapotranspiration of crops under predefined boundary conditions for the surface temperature where the latent heat flux reaches the maximum and minimum gradients. It is a recent methodology that sought to simplify the application of the process. Like the other methods, it was also validated by measurements using lysimeters (Senay *et al.*, 2014). Several studies have demonstrated the potential of the SSEBop model in estimating evapotranspiration in the evaluated locations (Senay *et al.*, 2014; Singh *et al.*, 2014; Senay *et al.*, 2016, Paula *et al.*, 2019; Vale *et al.*, 2022). Although the SSEBop model has been successfully applied using orbital sensors, there are still few studies using these models in high-resolution space-time images obtained by RPAs, especially for major agricultural crops.

Considering the Brazilian agricultural scenario, soybean (Glycine max L.) is a crop that occupies a prominent position in Brazilian agricultural production. The soybean planted area in the country grew 4.5% compared to the 2020/2021 crop, occupying an area of 40, 950.5 thousand ha. The estimated production for 2021/2022 crop was 124 million tons, with a reduction of 10.2% compared to the previous crop due to adverse weather conditions in the country's south at the end of 2021 (CONAB, 2021).

Given the importance of soybean crops and the relevance of determining the water demand for crops, the objective of this study is to apply the SSEBop model to estimate evapotranspiration using multispectral and thermal images obtained by an RPA in an experimental area cultivated with soybean.

2. Materials and Methods

The work was carried out using part of the plant phenotyping experiment for drought tolerance that takes place annually in the experimental field of Embrapa Cerrados in Planaltina - DF. These experiments are carried out with strict controls on materials and procedures. More details on the construction of the phenotyping experiment can be found in Pereira *et al.* (2021) and Tavares *et al.*

(2022). Thus, the experimental field and the details of the materials and methods that are directly linked to the remote sensing part are briefly described to achieve the objectives of this study.

2.1. Experimental field

The study was conducted at the Experimental Field of Embrapa Cerrados, in Planaltina, DF (15°36'00.3" S, 47°42'46.1," W and altitude 1006 m) (Fig. 1). Plant phenotyping experiments in this area are conducted annually to select materials tolerant to water stress. Sugarcane, coffee, wheat and soybean cultivars are evaluated in this area (Pereira *et al.*, 2021; Tavares *et al.*, 2022; Silva *et al.*, 2022).

The climate of the region is Aw (Köppen-Geiger) -Tropical type, with a well-defined dry period during the winter (May to September) (Alvares, 2013). The average annual rainfall in the region is 1542 mm, occurring mainly between October and April (Climate-Data, 2020). The weather data used in the experiment were collected through the Embrapa Cerrados meteorological station, 150 m from the experiment. The accumulated precipitation and average temperature for 2019 are shown in Fig. 2. This climatic characteristic is ideal for carrying out the experiment, given the prolonged dry period during the development of the experiment.

The soil of the experimental area is classified as dystroferric Red Latosol (clay = 46 g kg^{-1}, silt = 10 g kg^{-1} and sand = 42 g kg^{-1}) (Santos *et al.*, 2018). Fertilization was performed according to previous soil analysis and recommendations for the crop. For fertilization, 300 kg ha^{-1} of fertilizer formulated 04-30-16 (N, P$_2$O$_5$, K$_2$O) was used. In addition, phytosanitary treatments were conducted as needed and following the recommendations for the crop.

The experimental design adopted was randomized blocks in a split-plot scheme. In the plots, the six soybean
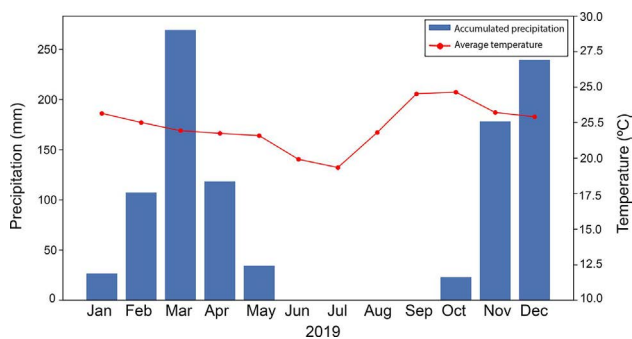

Figure 2 - Climatological data for the year 2019.

cultivars were tested (NA5909GR; M7190; BRS5980; BRS7180; BRS7280; BRS7380), which are in the maturation group between 6.9 and 7.3 and in the subplots the four water regimes (19, 42, 73 and 100 % of crop evapotranspiration - ETc), with three replications. Sowing took place on May 23, 2019, in a no-tillage system using 16 seeds per meter, deposited at a depth of 4 cm (Pereira *et al.*, 2021). Each experimental unit consisted of 36 cultivation lines of each cultivar, 5.0 m long, spaced 0.5 m apart. Each water regime (WR) constituted an experimental subunit of 5.0 m in length, formed by eight lines, with a spacing of 0.50 m. The useful area comprised the two central lines, discarding the borders and 0.5 m from each end. Figure 3 presents a sketch of the experimental area. The areas (1 m × 1 m) used to evaluate the aerial images obtained in the study are highlighted. For the evaluations by image, the average of the pixels of the indicated region were considered.

2.2. Irrigation management

The irrigation of the experiment was conducted using an irrigation bar (Irriga Brasil model 36/46), 20 m
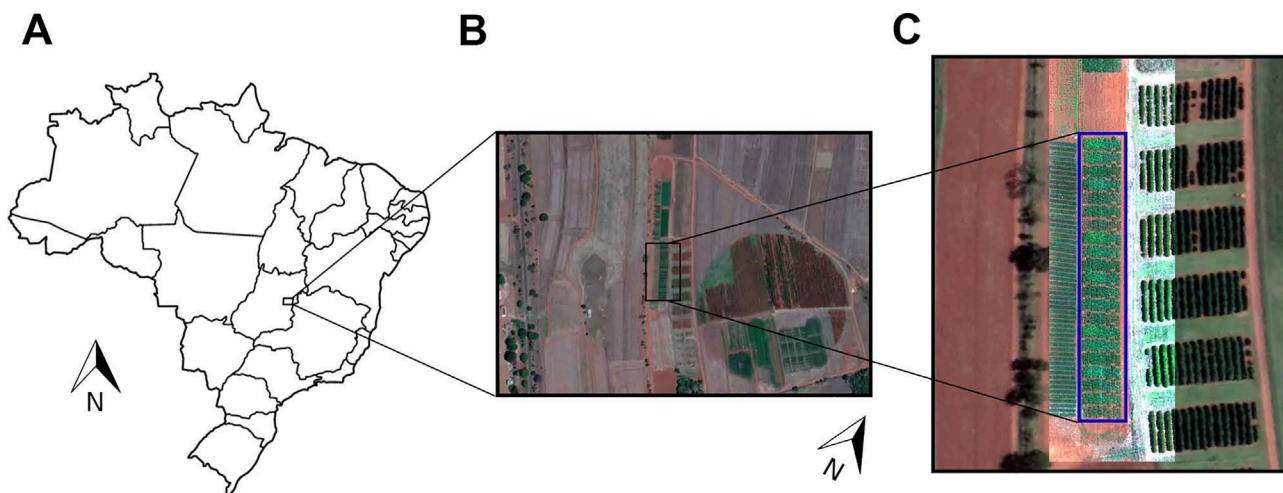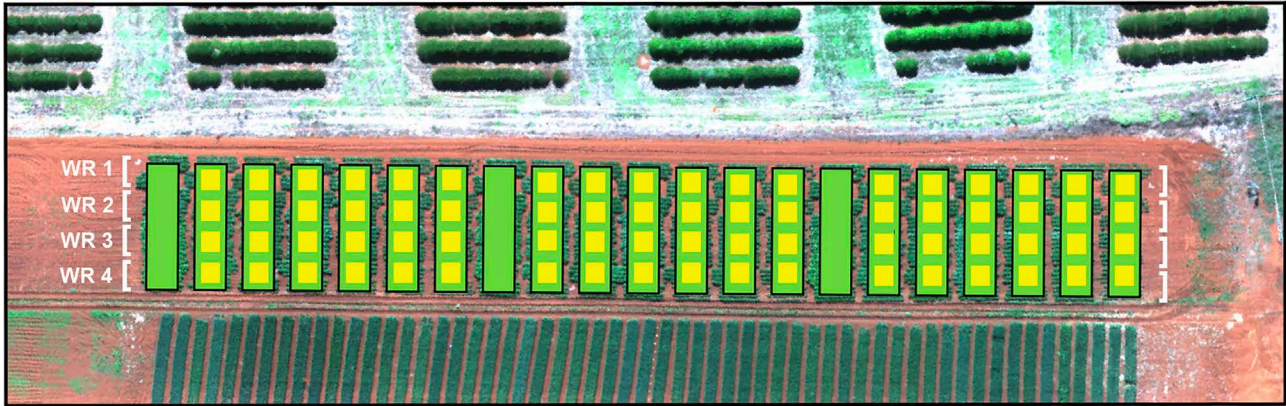

Figure 1 - Location of the study area (A- Planaltina, Distrito Federal, Brazil, B- Image of the location of the experimental area of EMBRAPA Cerrados in July 2019 and C - Aerial image of the experiment with soybean genotypes cultivated under different water regimes.

Figure 3 - Sketch of the soybean experimental area showing the distribution of the water regimes (WR) and the evaluation areas (1m × 1m) used in the image evaluations represented by the yellow squares.

wide on each side, connected to a TurboMaq 75/GB self-propelled engine with adjustable speed according to the water regime to be applied. (Fig. 4A). This bar moves over the entire experiment by applying the water depth that is previously configured (Jayme-Oliveira *et al.*, 2017). Irrigation is adjusted in two ways: by calibrating the flow of the sprinklers and through the displacement speed.

The irrigation depth applied is measured at each irrigation through 18 collector cups with 8 cm in diameter positioned immediately above the plants. These collectors were distributed parallel to the line to the irrigation bar, obtaining measurements every meter (Fig. 4 B). Immediately after irrigation, these collectors are emptied, and the volume collected is noted. These notes, together with the evapotranspiration calculated through data from the meteorological station, guide the following irrigations. Table 1 presents the irrigation depths and water regimes (WR) during the soybean crop cycle. Figure 4C shows a sketch of the irrigation bar and the differential irrigation zones defined for the experimental samples.
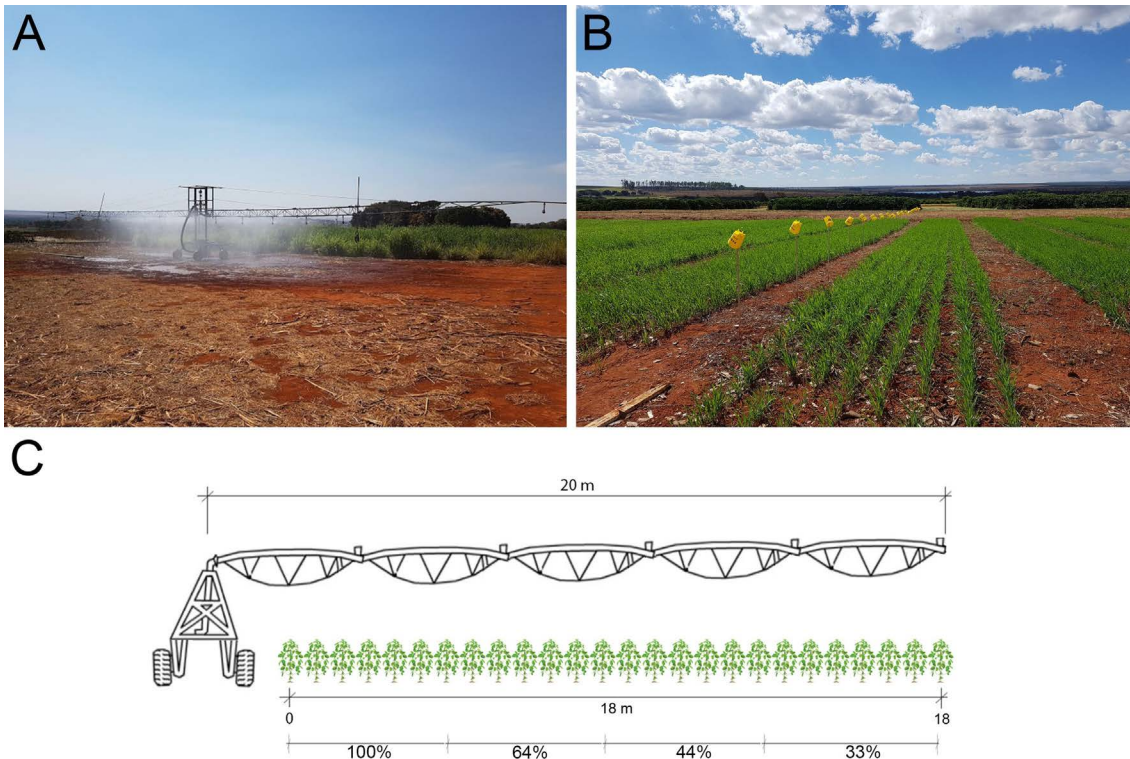
Figure 4 - Irrigation system. (A), Differential irrigation bar, (B) Collectors for quantification of the applied irrigation depth and Sketch of the irrigation bar showing the different irrigation sectors (C).

Table 1 - Irrigation depth applied in each water regime evaluated.

Water regime	Irrigation depths applied (mm) / DAS																					Total
	11	15	20	26	32	36	40	41	46	50	55	60	73	69	74	78	83	89	92	97	102	
WR 1 (19.3%)	11.7	7.4	9.4	11.8	18.8	15.1	7.7	11.3	3.1	0.1	1	3.8	2.3	2.6	1.6	0	0.7	0	0	0	0	108.4
WR 2 (42.5%)	13.5	9.3	11.3	13.5	22	17.6	9.9	14.3	13.5	7.8	9.8	16.8	13	15.7	12..9	8	11.3	3.4	2.7	7.2	4.8	233.5
WR 3 (73.5%)	14.6	9.8	11.4	15.8	22.9	17.6	9.9	13.5	23.3	17.6	21	29	23.6	28.5	24.5	28	28.7	19.1	12.6	21.9	18.8	393.3
WR 4 (100%)	15.4	9.9	12.6	17.1	26.8	20.3	10.3	13	29.7	23.3	28.1	38.2	29.4	38.7	19.4	45.1	34.6	43.4	19.6	39.5	34.6	526.4

The irrigation of the experiment was kept uniform for 41 days after sowing (DAS) with an average replacement of 120 mm of water. After this period, the sprinklers were adjusted to a decreasing flow, producing an irrigation gradient. The maximum level of irrigation applied was calculated according to the Cerrado irrigation monitoring program (Embrapa, 2016), which considers the climatic data of the region, crop evapotranspiration and irrigation schedule to calculate the amount of water needed, using an efficiency of 90%. The irrigation frequency was approximately 5 days, according to the climatic conditions and phenological stage of the crop.

2.3. Acquisition of the images

The images were captured using a remotely piloted aircraft (RPA) DJI model M600 hexacopter (SZ DJI Technology Co.) with an autonomy of 30 min of flight and a load capacity of up to 3 kg.

The multispectral images were acquired using a multispectral sensor brand Micasense model RedEdge. The sensor captures images in five spectral bands, called Blue (range: 465-485 nm; width: 20 nm), Green (range: 550-570 nm; width: 20 nm), Red (range: 663-673 nm; width: 10 nm), Red Edge (range: 712-722 nm; width: 10 nm), Near Infra-Red (NIR) (range: 820-860 nm; width: 40 nm)). It has a resolution of 1280×960 pixels for each band. The images were recorded in 12-bit RAW format (Micasense, 2020).

A FLIR DUO PRO R sensor (FLIR Systems, Danderyd, Sweden) was used to acquire the thermographic images: 730×480 spatial resolution, spectral response of 7.5 to 13.5 μm, uncooled microbolometer detector, 30 Hz frame rate, thermal sensitivity of < 50 mK, accuracy of 5 °C or 5% (whichever is greater) at 25° and weight of 325 g. The camera was configured for the environmental conditions at the time of image capture following the thermography principles presented by Usamentiaga *et al.* (2014), which include ambient temperature, imaging object distance, plant emissivity, reflected temperature and humidity. Thermographic images were saved in radiometric JPEG format.

Five flights were performed on 07/18, 07/25, 08/02, 08/12 and 08/21, 2019, between 10 am and 12 noon (GMT +3). Two flights were performed: one for acquiring multispectral images and another in sequence for the thermo-graphic images. Both flights were planned using DJI GS Pro software that allows creating a flight plan where the aircraft travels through pre-defined points guided by the GNSS system. The flight plans ensured that the capture was done with a minimum side and frontal overlap of 75% for the multispectral and 90% for the thermographic, maintaining a flight line at 100 m above ground level for the multispectral and 60 m for thermography.

2.4. Pre-processing of the images

The images collected by the cameras were imported and processed using the Pix4D Mapper software (Pix4D, Lausanne, Switzerland). Orthomosaics containing reflectance (multispectral) or temperature (thermal) values were computationally generated by the Structure from Motion (SfM) photogrammetric technology. SfM works with the automatic identification of similar features in a set of overlapping images through a packet adjustment procedure (Westoby *et al.*, 2012). Considering overlapping images, Pix4D Mapper calculates reflectance values for each pixel of the orthomosaic using a weighted average of pixels in all original images that correspond to this specific pixel but assigning more weight to images where the pixel is more central. The image pixel value depends on several factors, including sensor settings, sensor properties and scene conditions (Olivetti *et al.*, 2020).

For the multispectral sensor, radiometric corrections are applied to improve data quality using camera parameters, irradiance and corrections through the calibration panel. Along with these parameters, the software uses a photo of a calibration panel captured at the beginning of each flight and irradiance information collected by the solar sensor for data normalization. Thus, it is possible to compare the images captured in different lighting conditions.

Figure 5 presents in a simplified way the main processing steps using Pix4D. The location of the captured and imported images is shown in Fig 5A, followed by the 3D point cloud generated in Fig 5B, and finally, the calibrated orthomosaic in Fig 5C. The choice of software adjustment parameters was made following information provided by the software documentation and camera manufacturer recommendations (Pix4D, 2020; Micasense, 2020).

The reflectance orthomosaics generated in Pix4D were imported into the QGIS software, where the images
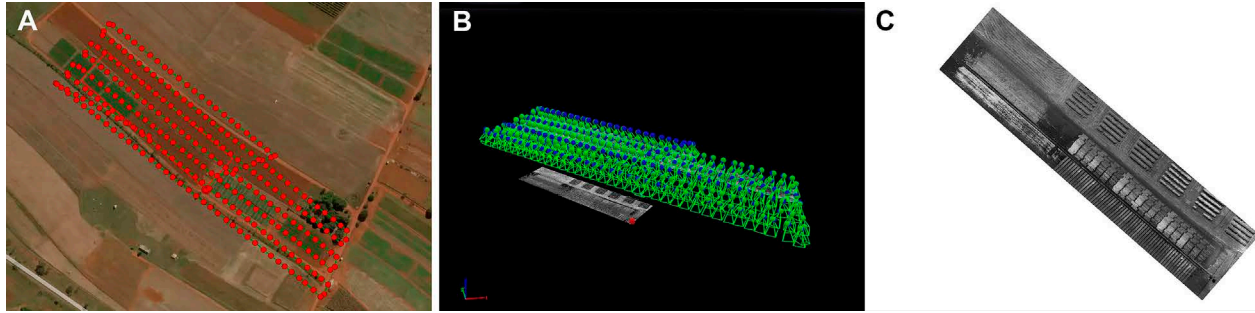
Figure 5 - Simplified process for the construction of orthomosaics. (A) Position of captured and imported images. (B) Alignment of images by triangulation. (C). Multispectral orthomosaic of the assay.

were cropped to present only the area of interest containing the soybean genotypes. The NDVI vegetation index was calculated using the QGIS raster calculator, with Eq. (5) (Rouse *et al.*, 1973).

For the georeferencing of all orthomosaics, five ground control points were used, which were painted in the shape of an arrow at the borders of the experimental area. The QGIS image georeferencing tool was used for the process, and the multispectral image from 07/25/2019 was selected as the location reference image. So all other images were georeferenced based on the geolocation of that image.

The thermographic images were also aligned and transformed into orthomosaic using Pix4D, but with the Thermal processing mode. The procedures and recommendations described in the Pix4D software documentation (2019) and the calibration principles used by Usamentiaga *et al.* (2014) and Casari *et al.* (2019) were followed.

2.5. Evapotranspiration estimated by the SSEBop model

To determine the evapotranspiration fraction (*ETf*) by the SSEBop method, multispectral images in the visible, near infrared and thermal ranges, and local meteorological data, were used. Unlike the original proposal of the work by Senay *et al.* (2013), the images used were not obtained by satellite but by a remotely piloted aircraft at low altitude. The estimate of real evapotranspiration through the SSEBop model (*ETrSSEBop*) is obtained by multiplying the dimensionless evapotranspiration fraction (*ETf*) for a scale factor (*k*) and by the reference evapotranspiration (*ETo*) calculated by the Penman-Monteith-FAO method for grass, according to Eq. (1):

$$ETr_{SSEBop} = ETf \cdot k \cdot ETo \qquad (1)$$

According to Senay *et al.* (2013), a value for *k* of 1.2 is indicated, equivalent to an aerodynamically rougher surface than grass. However, this coefficient can be determined in the field, based on the vegetation of the area, or

validated/calibrated from water balance data. The fraction of evapotranspiration in a pixel can be calculated by Eq. (2), where *Ts* is the surface temperature of the pixel observed by the thermographic image obtained by remote sensing; *Th* is the estimated surface temperature of the dry/warm boundary condition for the same pixel; and *dT* is the temperature difference of the boundary conditions *Tc* and *Th (dT = Th - Tc)* at each pixel. Values with negative *ETf* are converted to zero, and their maximum value measure is restricted to 1.05. Senay *et al.* (2016) recommends that pixels with the presence of clouds be disregarded from the processing; however, as we are working with images of low flight altitude and in a dry period, there is no need to disregard these pixels:

$$ETf = \frac{Th - Ts}{Th - Tc} = \frac{Th - Ts}{dT} \qquad (2)$$

The *Tc* value is calculated from the air temperature, according to Eq. (3), where *Tmax* is the maximum air temperature on the day of the evaluation, and c is a correction factor that relates *Tmax* and *Ts* on a well-vegetated surface with good water availability. (Senay *et al.*, 2016).

$$Tc = c \times Tmax \qquad (3)$$

where:

$$c_{pixel} = \frac{(Ts|NDVI \geq 0.8)}{Ta} \qquad (4)$$

and *NDVI* is calculated by the equation:

$$NDVI = \frac{NIR - Red}{NIR + Red} \qquad (5)$$

where $Ts|NDVI \geq 0.8$ is the surface temperature where the *NDVI* is greater than 0.8, and *Ta* is the air temperature at the time of the evaluations. The temperature differential *dT* is determined by solving the energy balance equation (Eq. (6)) for exposed and dry soil, representing the dry/warm boundary condition. Where *Rn* is the net radiation in the study area, *LE*

is the latent heat; H is sensible heat; G is the heat flux in the soil; µa is the density of air, Cp is the specific heat of air; and rah is the aerodynamic drag for exposed, dry ground. Considering LE and G equal to zero, we have dT given by Eq. (7) (Allen *et al.*, 2007; Bastiaanssen *et al.*, 1998).

$$Rn = LE + H + G \approx H = \frac{\rho a \cdot Cp \cdot dT}{rah} \quad (6)$$

$$dT = \frac{Rn \times r_{ah}}{\rho a \times Cp} \quad (7)$$

The hot pixel condition Th is then calculated by Eq. (8):

$$Th = Tc + dT \quad (8)$$

After the alignment between the orthomosaics, the images were imported by the script developed in Python programming language to calculate the evapotranspiration through the SSEBop model. To run the script, the Jupyter notebook platform was used (Kluyver *et al.*, 2016). Figure 6 presents a flowchart of the SSEBop model implementation.
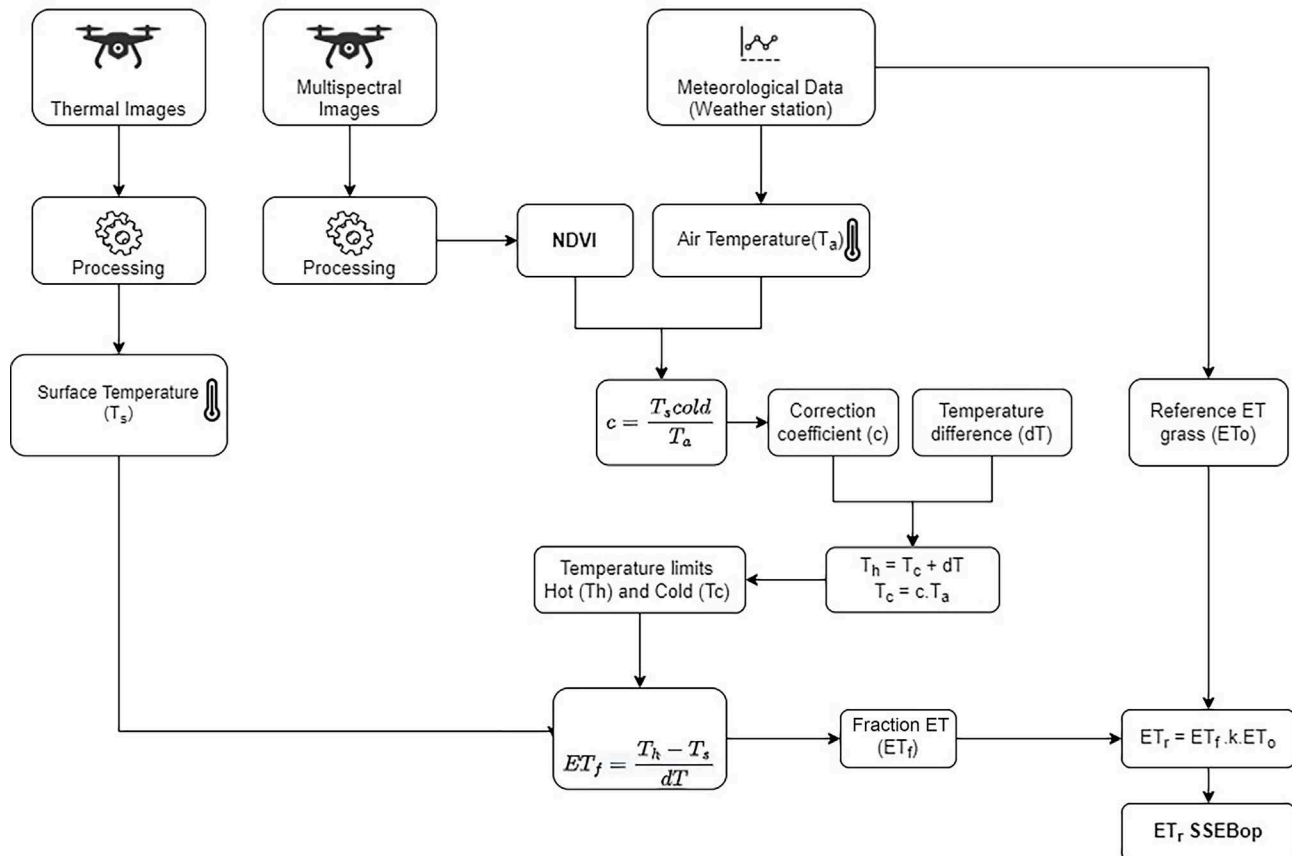
2.6. Meteorological data

The meteorological data necessary for the application of the SSEBop model and for the determination of the irrigation depth were obtained through the meteorological station of EMBRAPA Cerrados, in Planaltina - DF, with the following geographic location: 15°36'4.91" S, 47°42'48.47" W, being located 150 m from the study area.

The SSEBop model uses the FAO 56 Penman-Monteith equation (Allen *et al.*, 1998) to estimate the daily ETo to determine the ETr, according to Eq. (8). The reference evapotranspiration was calculated according to Eq. (9)

$$ETo = \frac{0.408\Delta(Rn - G) + \gamma\left(\frac{900}{tmed + 273}\right)u2(e_s - e_a)}{\Delta + \gamma(1 + 0.34u_2)} \quad (9)$$

The processing of data from the meteorological station and the calculation of *ETo* by the Penman-Monteith FAO 56 method was performed using a code written in Python using the reference equations.

2.7. Gas exchanges

To characterize the physiological variables of gas exchange, an infrared gas analyzer IRGA model LI-

Figure 6 - Processing flowchart of the ETr estimate by the SSEBop model.

7300XT (LI-COR, Inc., Lincoln, NE, USA) was equipped with a measuring head measuring 2×3 cm and a Model 7300-02B LED artificial lighting system.

The relative humidity of the evaluation head was set at 50-60%, light intensity at 1200 µmol m^{-2} s^{-1}, block temperature at 30 °C, flow at 500 µmol s^{-1} and the reference CO_2 concentration was controlled at 400 ppm. The following variables were evaluated: net CO_2 assimilation (*A*), stomatal conductance (*gs*) and transpiration rate (*E*).

During the soybean cycle, an evaluation was performed 89 days after sowing (DAS). In each plot, three evaluations were performed to quantify gas exchange. The evaluations were performed on the central leaf of the fully expanded trifoliate using physiologically mature soybean leaves (Valdez *et al.*, 2014).

3. Results and Discussions

3.1. Gas exchanges

Figure 7(A) shows the mean photosynthesis values observed in all genotypes evaluated at 89 DAS. Figure 7 (B) presents the leaf transpiration rate and Fig. 7(C) presents the stomatal conductance values for the same date.

Treatments with 100% (WR4) and 73% (WR3) irrigation showed higher values of photosynthesis and transpiration rate than treatments with lower water replacement (WR2 and WR1), differing statistically by Tukey's test. The WR4 and WR3 levels showed average photosynthesis of 25.23 and 23.59 µmol CO_2 m^2 s^{-1}, respectively, while the WR2 and WR1 levels showed averages of 12.19 and 4.47 µmol CO_2 m^2 s^{-1}. This similar trend is observed in the values of leaf transpiration rate, where the highest levels present values of 6.77 and 5.90 H_2O m^2 s^{-1} for the RH4 and WR3 levels and 2.25 and 0.68 mmol H_2O m^2 s^{-1} for WR2 and WR1 levels, respectively. The reduction in photosynthetic rate, leaf transpiration rate, and stomatal conductance (Fig. 7C) is expected as a function of water deficit because the uptake of CO_2 is reduced (Godoy Androcioli *et al.*, 2020) and senescence induced by water restriction (Munné-Bosch and Alegre, 2004). Plants under water stress decreases photosynthesis due stomatal closure, which reduces cells expansion, leading

to lower leaf elongation and as a consequence lower leaf area, biomass accumulation and lower yield (Jones, 1990; Parkash and Singh, 2020).

3.2. NDVI

The average values of NDVI for the experimental plots (1 m × 1 m) are shown in Fig. 8. The time series evaluated presents the highest value point for all water regimes in DAS 63 due to natural senescence, which is more expressive and accelerated for plants with lower water depth replacement. The plots with irrigation depths of 100% (WR4 and 73% (WR3) showed minor difference between them when compared with the water depths of 19% (WR2) and 42% (WR1).

The behavior of the NDVI for the soybean cycle with 100% (WR4) and 73% (WR3) of water replacement followed the normal cycle of the culture, presenting in the initial phase, an increase of the NDVI with the vegetative development of the plants until reaching a maximum level for the management conditions of the experiment when there is greater leaf area and vegetative vigor, in which it stabilizes for a period and later there is a decline indicating physiological maturation. In the sectors with replacement of 42% (WR2) and 19% (WR1) of evapotranspiration, there was an early reduction of the index, if compared to the replacement of 100% (WR4), indicating a stress beha-
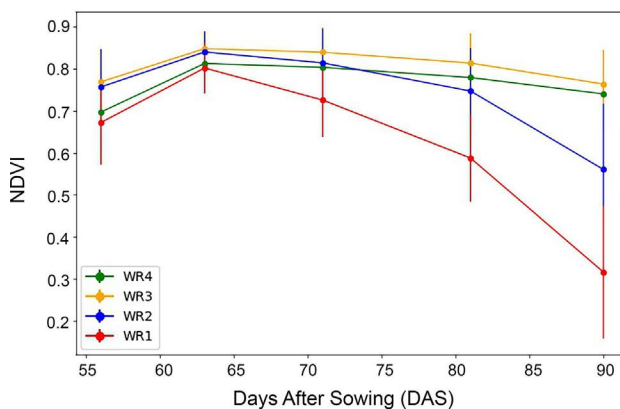
Figure 8 - NDVI curves for different water regimes during the soybean crop cycle.
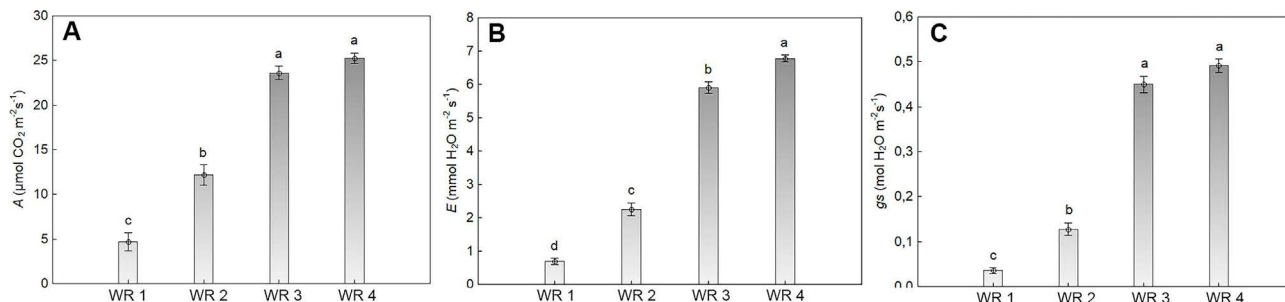
Figure 7 - Gas exchanges. (A) Photosynthesis, (B) Leaf transpiration rate and (C) Stomatal conductance for the DAS 89 assessment.

vior of the plants. This stress can be observed in Fig. 9 and in the field with anticipation of the cycle, chlorosis, and size reduction.

The use of NDVI through precision agriculture has great application in agriculture because it is an non-invasive methodology, and easy evaluation (Crusiol *et al.*, 2017) and can be used in the cultivation of irrigated soybean, sustainable management of water resources. The NDVI is sensitive to leaf pigments, especially the chlorophyll content of the leaves; in addition, it correlates with the photosynthetic rate, stomatal conductance, transpiration and soybean productivity (Tavares *et al.*, 2022) in Future can replace physiological evaluations that are laborious and time consuming. NDVI can estimate Leaf area index, plant biomass and water stress (Tian *et al.*, 2017; Zhu *et al.*, 2015; Silva *et al.*, 2016),

In this work, the data obtained by gas exchange and NDVI via remote sensing showed the same trends as gas exchange, that is, the water regimes WR1 and WR2 showed the lowest gas exchange (Fig. 7) and the lowest NDVI values, which may facilitate the use of this index in areas under different water regimes.

3.3. Surface Temperature

The surface temperature is a crucial parameter for determining evapotranspiration by the SSEBop model. Figure 10 shows the surface temperature images collected on the same dates as the NDVI. Figure 11 shows the graph of the average temperature of the selected areas of the experimental plots (1 m × 1 m) throughout the cycle and in response to the evaluated water regimes.

An indicator of water stress in plants is the increase in canopy temperature, measured using portable thermographic sensors (Bian *et al.*, 2019; Casari *et al.*, 2019). Several studies concluded the existence of a significant negative correlation between canopy temperature and grain yield in plants under water deficit in the soil (Sirault *et al.*, 2009; Romano *et al.*, 2011; Prashar *et al.*, 2013; Silva *et al.*, 2023).

Analyzing the surface temperature of the soybean canopy in response to the application of water regimes, it is possible to observe a detachment between the curves in the first evaluation, which indicates the beginning of water stress in the sector with less irrigation. As the cycle progresses, there is an increase in surface temperature in the
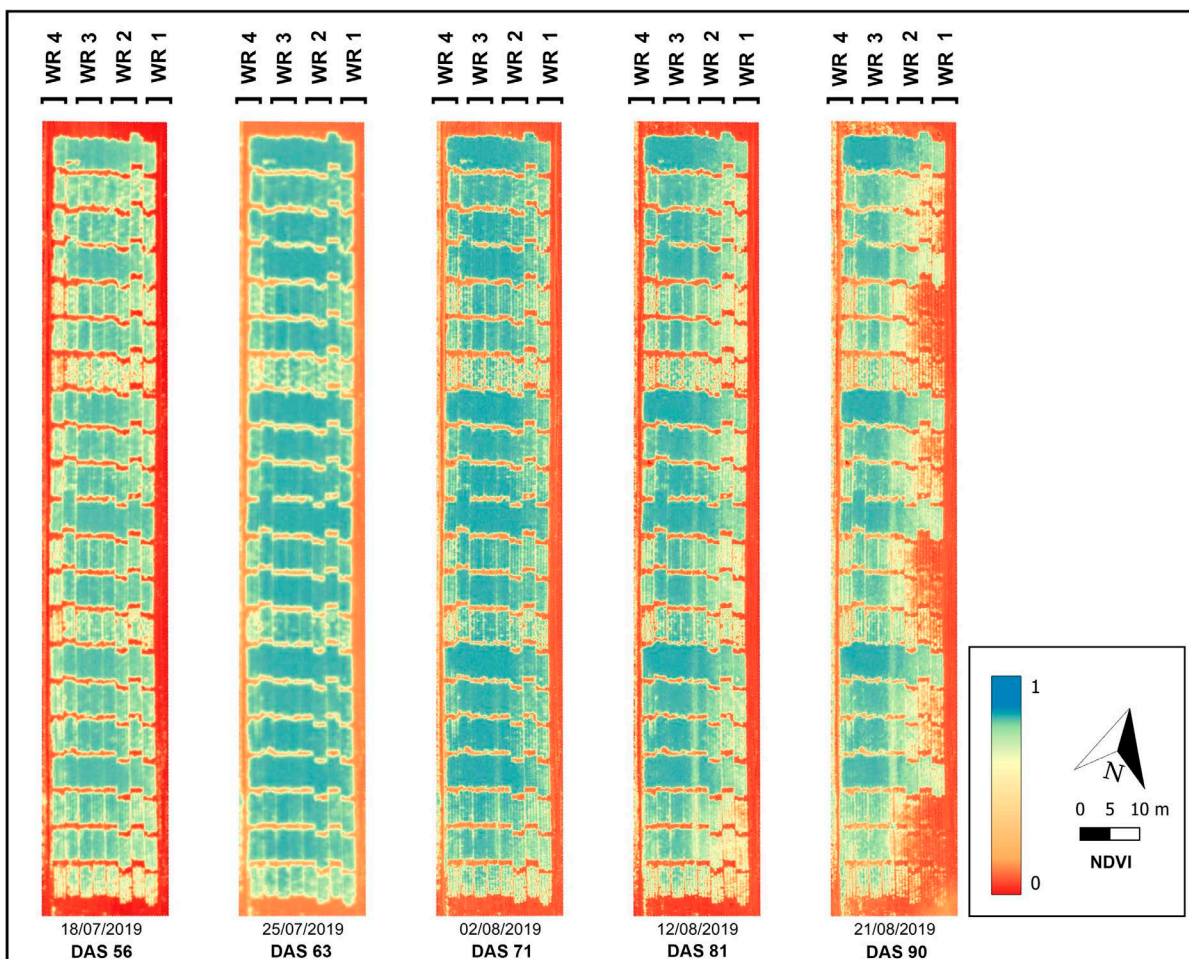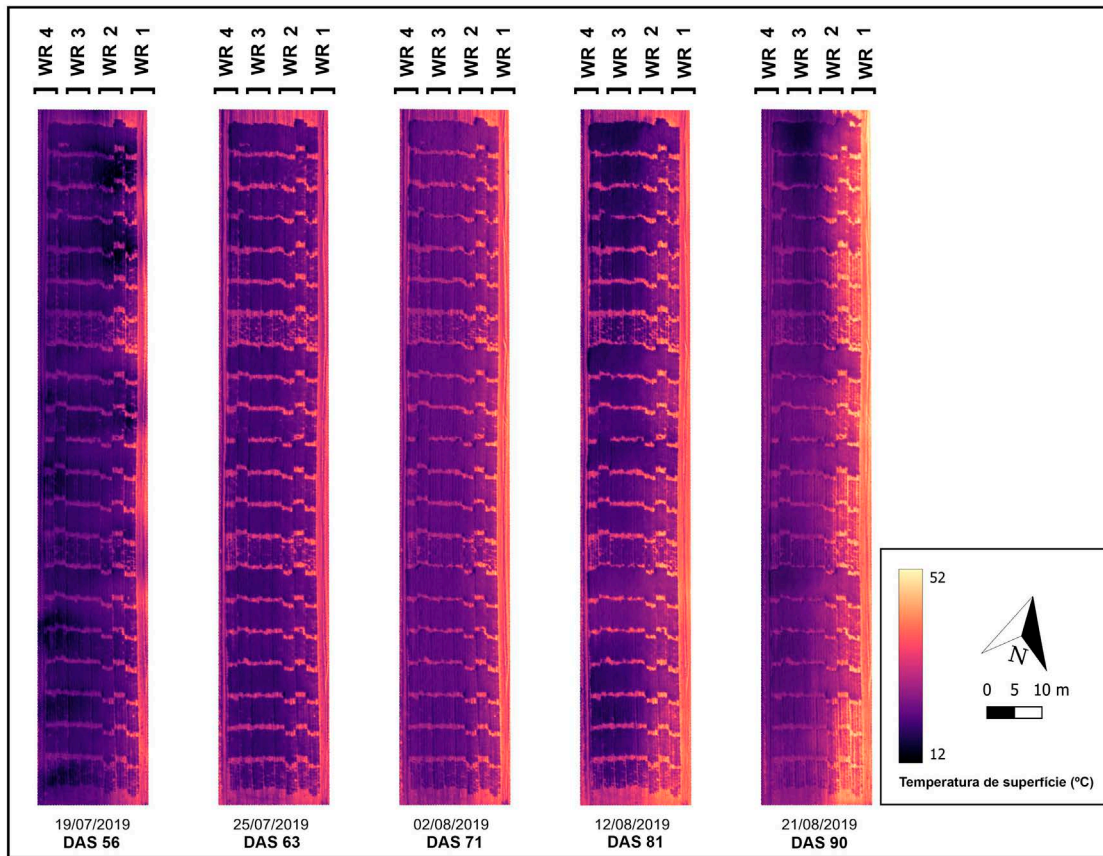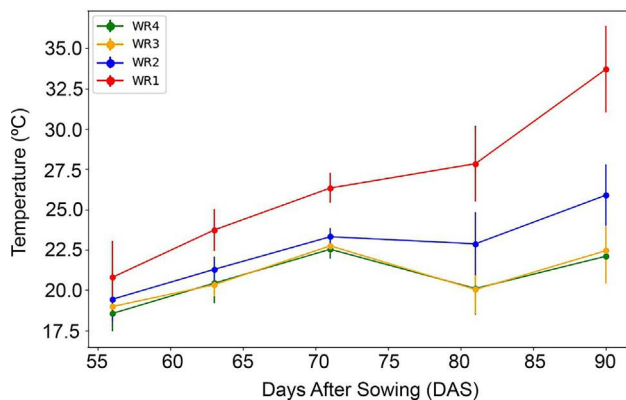

Figure 9 - NDVI maps for soybean in response to different water regimes. Planaltina, DF, 2019.

Figure 10 - Soybean canopy surface temperature maps in response to applied water regimes. Planaltina, DF, 2019.

Figure 11 - Soybean canopy surface temperature in response to applied water regimes.

sectors with 19% (WR1) and 42% (WR2) of water replacement in relation to the sectors with 73% (WR3) and 100% (WR4) of water replacement. The increase in temperature in these regions is expected due to stomatal closure of the plants, which causes a decrease in the foliar transpiration capacity and the consequent increase in temperature (Silva *et al.*, 2023). This control is an important physiological property through which plants limit water

loss, causing reductions in stomatal conductance and, generally, reducing gas exchange as a form of plant response to several factors, including water stress (Paiva *et al.*, 2005; Silva *et al.*, 2023). The values of stomatal conductance (*gs*) as a function of the applied water regime are presented in Fig. 7(C) confirm the stomata closure for the more restricted water regimes. As the applied stress is prolonged, there is also a reduction in the size of the plants, with a decrease in leaf area and soil exposure in the images, which further increases the temperature of the microregion (Farooq *et al.*, 2009). Canopy temperature is also related to above-ground biomass production, water use efficiency in plants and yield (Silva *et al.*, 2023).
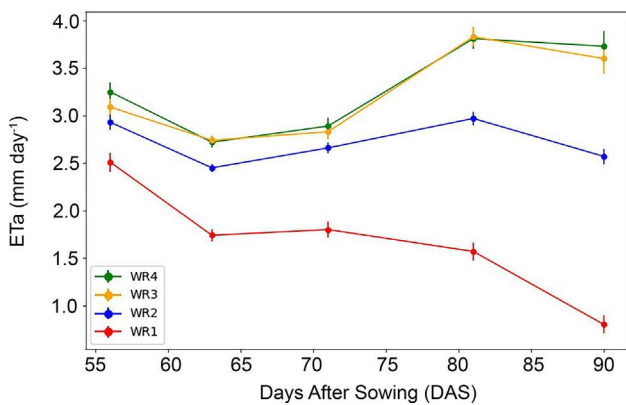
3.4. Evapotranspiration

Figure 12 shows the images of the daily evapotranspiration maps estimated by the SSEBop model along the cycle obtained through the multispectral images and surface temperature collected by ARP. Figure 13 presents the graph with the estimated values of crop evapotranspiration throughout the cycle. As in the surface temperature, there is a difference in the evapotranspiration of the sectors with 19% (WR1) and 42% (WR2) of water replacement in relation to the sectors with 73% (WR3) and
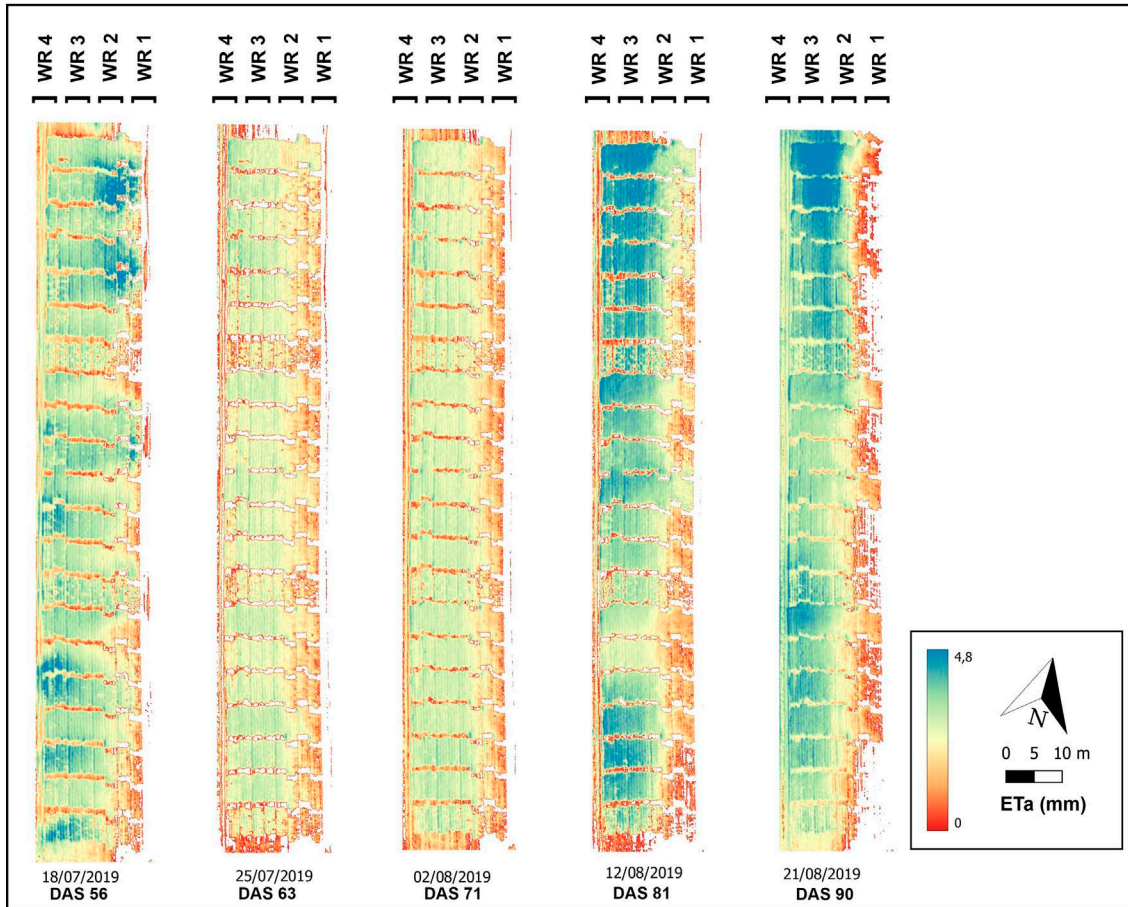
Figure 12 - Maps of real evapotranspiration estimated by the SSEBop model for soybean in response to the application of different water regimes. Planaltina, DF, 2019.
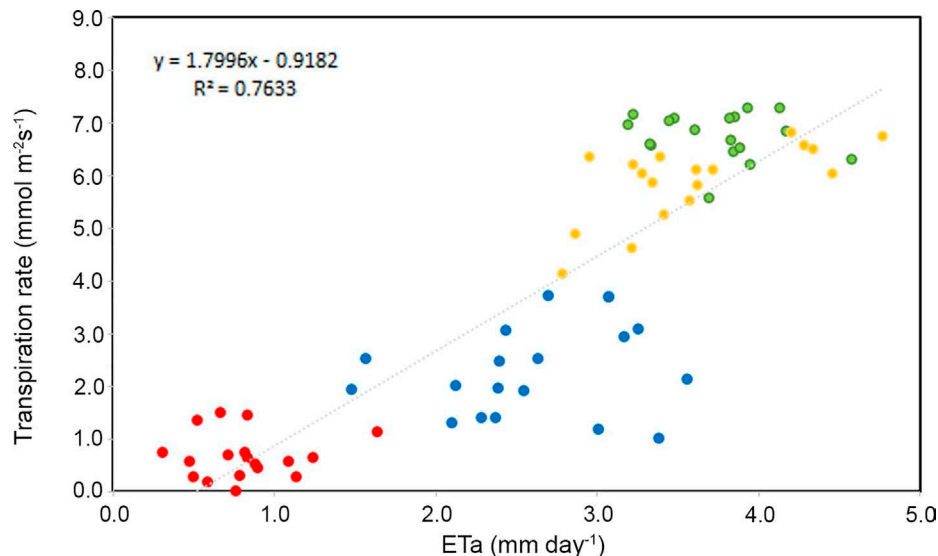

Figure 13 - Actual evapotranspiration estimated by the SSEBop model along the soybean cycle in response to the application of different water regimes.

100% (WR4) of the replacement of water. However, the 73% (WR3) and 100% (WR4) sectors remain without significant changes between them, while the 19% (WR1) and 73% (WR2) sectors show greater differences in relation to the material with 100% irrigation depth (WR4), which is expected as a function of proportional irrigation.

The actual evapotranspiration estimated by SSEBop was compared with the leaf transpiration rate (mmol m^2 s^{-1}). The estimated evapotranspiration in the DAS 90 evaluation showed a $R^2 = 0.76$ with the leaf transpiration rate obtained in the DAS 89 (Fig. 14). This comparison was performed considering the weather stability observed between the two days. The results indicate that the estimated evapotranspiration was positively correlated with the leaf transpiration measurements. Despite this correlation, the comparison only with transpiration at a point in time may not be the ideal method to determine the functioning of the model. It is necessary to emphasize that the ground truth considers only leaf transpiration, leaving open the factor of evaporation of the evaluated microregion. Although the data explain part of the factors, the study demonstrates the usefulness and functioning of the SSEBop model with the use of high-resolution images in research areas and production fields.

Regarding the variability found in the data obtained remotely, it is believed that the high resolution of the sensors can explain part of the variability found in the analyses, considering that the evaluation in different phenolo-

Figure 14 - Dispersion between leaf transpiration rate (mmol m^{-2} s^{-1}) and real soybean evapotranspiration estimated by the SSEBop model (mm day^{-1}). In red, genotypes submitted to WR1, in blue, genotypes submitted to WR2, in yellow, genotypes submitted to WR3 and in green, genotypes submitted to WR 4.

gical stages or different levels of water stress ends up also considering areas where canopy coverage is deficient or have a smaller leaf area. This ends up exposing an amount of soil and interfering with the evaluation of the numerical value of the pixel. Despite this, it is also understood that this soil interference is part of the physiological response process of the plant to stress. Despite the variability found, the estimated results compared with leaf transpiration show that the SSEBop model using high-resolution images has the potential to estimate evapotranspiration in experimental areas. This model can be explored in future experiments with different cultures and phenological stages.

4. Final Remarks

The study evaluated the possibility of using high-resolution multispectral and thermal images obtained by RPAs to estimate evapotranspiration in an experimental soybean field. Thermography and NDVI maps were generated as sources for estimating evapotranspiration. The use of the SSEBop model through high-resolution images is shown as a potential tool for water stress assessments in soybean crops. This work obtained a good linear correlation between estimated evapotranspiration and leaf transpiration. The results showed the possibility of transferring a model originally designed for low to medium-resolution images from remote sensing by satellites to high-resolution space-time images acquired by RPA, with small adaptations and generating great potential for scale-up field studies. We encourage the development of more studies using high-resolution images for different cultures and phenological stages to support a more robust evaluation.

Acknowledgments

References

ALLEN, R.G. Crop evapotranspiration. **FAO Irrigation and Drainage Paper**, v. 56, p. 60-64, 1998.

ALLEN, R.G.; TASUMI, M.; TREZZA, R. Satellite-based energy balance for mapping evapotranspiration with internalized calibration (METRIC) - Model. **Journal of Irrigation and Drainage Engineering**, v. 133, n. 4, p. 380-394, 2007.

ALVARES, C.A.; STAPE, J.P.; SENTELHAS, P.C.; GONÇALVES, J.D.M.; SPAROVEK, G. Köppen's climate classification map for Brazil. **Meteorologische Zeitschrift**, v. 22, n. 6, p. 711-728, 2013. doi

BASTIAANSSEN, W.G.M.; MENENTI, M.; FEDDES, R.A.; HOLTSLAG, A.A.M. A remote sensing surface energy balance algorithm for land (SEBAL). 1. Formulation. **Journal of Hydrology**, v. 212, p. 198-212, 1998. doi

BIAN. J.; ZHANG. Z.; CHEN. J.; CHEN. H.; CUI. C.; *et al.* Simplified evaluation of cotton water stress using high resolution unmanned aerial vehicle thermal imagery. **Remote Sensing**, v. 11, n. 3, 267, 2019. doi

BOUNOUH, O.; ESSID, H.; FARAH, I.R. Prediction of land use/land cover change methods: A study. In: **2017 International Conference on Advanced Technologies for Signal and Image Processing (ATSIP)**. IEEE, p. 1-7, 2017.

CASARI, R.A.C.N.; PAIVA, S.D.; SILVA. V.N.B.; FERREIRA. T.M.M.; SOUZA JUNIOR, M.T.; *et al*. Using thermography to confirm genotypic variation for drought response in maize. **International Journal of Molecular Sciences**, v. 20, n. 9, p. 2273, 2019. doi

CLIMATE-DATA.ORG. **Clima Brasília** (2021). Available in https://pt.climate-ata.org/america-do-sul/brasil/distrito-federal/brasilia-852/#climate-table, accessed on July 17, 2022.

CONAB. Acompanhamento da safra brasileira de grãos, Acompanhamento - safra de grãos, Brasília, v. 9 - Safra 2021/22, n.1 - Primeiro levantamento. In: **Boletim da Safra de Grãos**, Brasília: CONAB, p. 1-86, 2021.

CRUSIOL, L.G.T.; CARVALHO, J.F.C.; SIBALDELLI, R.N.R.; NEIVERTH, W.; RIO. A.; *et al.* NDVI variation according to the time of measurement, sampling size, positioning of sensor and water regime in different soybean cultivars. **Precision Agriculture**, v. 18, p. 470-490, 2017.

EMBRAPA. **Programa de Monitoramento da Irrigação**. Brasília: EMBRAPA, 2016. Available in https://hidro.cpac.embrapa.br/, accessed on July 17, 2018.

FRANCO, R.A.M.; HERNANDEZ, F.B.T.; TEIXEIRA, A.H.C.; FEITOSA, D.G. Avaliação do balanço de energia em diferentes tipos de uso e cobertura da terra na região noroeste do Estado de São Paulo. In: **SBSR Simposio Brasileiro De Sensoriamento Remoto**. p. 6909-6916, 2013.

ANDROCIOLI, L.G.; ZEFFA, D.M.; ALVES, D.S.; TOMAZ, J.P.; MODA-CIRINO, V. Effect of water deficit on morphoagronomic and physiological traits of common bean genotypes with contrasting drought tolerance. **Water**, v. 12, n. 1, p. 217, 2020.

JAYME-OLIVEIRA, A.; RIBEIRO JÚNIOR, W.Q.; RAMOS, M.L.G.; ZIVIANI, A.C.; JAKELAITIS, A. Amaranth, quinoa, and millet growth and development under different water regimes in the Brazilian Cerrado. **Pesquisa Agropecuária Brasileira**, v. 52, p. 561-571, 2017.

JIANYAA, G.; HAIGANGA, S.; GUORUIA, M.; QIMINGB, Z. A review of multi-temporal remote sensing data change detection algorithms. **The International Archives of the Photogrammetry, Remote Sensing and Spatial Information Sciences**, v. 37, n. B7, p. 757-762, 2008.

JONES, H.G. Physiological aspects of the control of water status in horticultural crops. **HortScience**, v. 25, n. 1, p. 19-25, 1990.

KARIMI, P.; BASTIAANSSEN, W.G.M. Spatial evapotranspiration, rainfall and land use data in water accounting-Part 1: Review of the accuracy of the remote sensing data. **Hydrology and Earth System Sciences**, v. 19, n. 1, p. 507-532, 2015.

KLUYVER. T.; RAGAN-KELLEY, B.; PÉREZ, F.; GRANGER, B.; BUSSONNIER, M.; FREDERIC, J.; *et al.* Jupyter notebooks - A publishing format for reproducible computational workflows. **Elpub**, v. 2016, p. 87-90, 2016. doi

MICASENSE. How to process MicaSense sensor data in Pix4D. 2020. Available in https://support.micasense.com/hc/en-us/articles/115000831714-How-to-Process-MicaSense-Sensor-Data-in-Pix4D, accessed on July 17, 2022.

MUNNÉ-BOSCH, S.; ALEGRE, L. Die and let live: leaf senescence contributes to plant survival under drought stress. **Functional Plant Biology**, v. 31, n. 3, p. 203-216, 2004.

OLIVETTI, D.; ROIG, H.; MARTINEZ, J-M.; BORGES, H.; FERREIRA, A.; CASARI, R.; *et al.* Low-cost unmanned aerial multispectral imagery for siltation monitoring in reservoirs. **Remote Sensing**, v. 12, n. 11, p. 1855, 2020.

PAULA, A.C.P. de; SILVA, C.L. da; RODRIGUES, L.N.; SCHERER-WARREN, M. Performance of the SSEBop model in the estimation of the actual evapotranspiration of soybean and bean crops. **Pesquisa Agropecuária Brasileira**, v. 54, e00739, 2019. doi

PAIVA, A.S.; FERNANDES, E.J.; RODRIGUES, T.J.D.; TURCO, J.E.P. Condutância estomática em folhas de feijoeiro submetido a diferentes regimes de irrigação. **Engenharia Agrícola**, v. 25, p. 161-169, 2005.

PARKASH, V.; SINGH, S. A review on potential plant-based water stress indicators for vegetable crops. **Sustainability**, v. 12, n. 10, e3945, 2020.

PEREIRA, L.F.; RIBEIRO, W.Q.; RAMOS, M.L.G.; SANTOS, N.Z.; SOARES, G.F.; CASARI, R.A.C.N.; *et al.* Physiological changes in soybean cultivated with soil remineralizer in the Cerrado under variable water regimes. **Pesquisa Agropecua?ria Brasileira**, v. 56, p. e01455, 2021.

PIX4D. **Step 4 - Processing**. 2020. Available in https://support.pix4d.com/hc/en-us/articles/204272989-Offline-Getting-Started-and-Manual-pdf, access on May 15, 2022.

PRASHAR, A.; YILDIZ, J.; MCNICOL, J.W.; BRYAN, G.J.; JONES. H.G. Infra-red thermography for high throughput field phenotyping in Solanum tuberosum. **PLoS One**, v. 8, n. 6, p. e65816, 2013.

ROMANO, G.; ZIA, S.; SPREER, W.; SANCHEZ, C.; CAIRNS, J.; ARAUS, J.L.; MÜLLER, J. Use of thermography for high throughput phenotyping of tropical maize adaptation in water stress. **Computers and Electronics in Agriculture**, v. 79, n. 1, p. 67-74, 2011. doi

ROUSE, J.W.; HAAS, R.H.; SCHELL, J.A.; DEERING, D.W. Monitoring vegetation systems in the great plains with ERTS. **NASA Spec. Publ**, v. 351, n. 1, p. 309, 1974.

SANTOS, H.G.; JACOMINE, P.K.T.; ANJOS, L.H.C.; OLIVEIRA, V.A.; LUMBRERAS, J.F.; *et al.* **Sistema Brasileiro de Classificação de Solos**. Brasília: Embrapa, 2018.

SENAY, G.B.; BOHMS, S.; SINGH, R.K.; GOWDA, P.H.; VELPURI, N.M.; ALEMU, H.; VERDIN, J.P. Operational evapotranspiration mapping using remote sensing and weather datasets: A new parameterization for the SSEB approach. **JAWRA Journal of the American Water Resources Association**, v. 49, n. 3, p. 577-591, 2013. doi

SENAY, G.B.; FRIEDRICHS, M.; SINGH, R.K.; VELPURI, N.M. Evaluating Landsat 8 evapotranspiration for water use mapping in the Colorado River Basin. **Remote Sensing of Environment**, v. 185, p. 171-185, 2016. doi

SENAY, G.B.; GOWDA, P.H.; BOHMS, S.; HOWELL, T.A.; FRIEDRICHS, M.; *et al.* Evaluating the SSEBop approach for evapotranspiration mapping with landsat data using lysimetric observations in the semi-arid Texas High Plains. **Hydrology and Earth System Sciences Discussions**, v. 11, n. 1, p. 723-756, 2014. doi

SILVA, P.C. da; RIBEIRO JUNIOR, W.Q.; RAMOS, M.L.G.; ROCHA, O.C.; VEIGA, A.D.; *et al.* Physiological changes

of Arabica Coffee under different intensities and durations of water stress in the Brazilian Cerrado. **Plants**, v. 11, n. 17, p. 2198, 2022.

SILVA, G.F.C.; GONCALVES, A.C.A.; SILVA JUNIOR, C.A.; NANNI, M.R.; FACCO, C.U. *et al.* NDVI response to water stress in different phenological stages in culture bean. **Journal of Agronomy**, v. 15, n. 1, p. 1-10, 2016. doi

SILVA, A.N.; RAMOS, M.L.G.; RIBEIRO JUNIOR, W.Q.; SILVA, P.C. da; SOARES, G.F.; CASARI, R.A.C.N.; *et al.* Use of thermography to evaluate alternative crops for off-season in the cerrado region. **Plants**, v. 12, n. 11, p. 2081, 2023.

SINGH, A. Conjunctive use of water resources for sustainable irrigated agriculture. **Journal of Hydrology**, v. 519, p. 1688-1697, 2014.

SIRAULT, X.R.R.; JAMES, R.A.; FURBANK, R.T. A new screening method for osmotic component of salinity tolerance in cereals using infrared thermography. **Functional Plant Biology**, v. 36, n. 11, p. 970-977, 2009. doi

SISHODIA, R.P.; RAY, R.L.; SINGH, S.K. Applications of remote sensing in precision agriculture: A review. **Remote Sensing**, v. 12, n. 19, p. 3136, 2020.

SU, Z. The Surface Energy Balance System (SEBS) for estimation of turbulent heat fluxes. **Hydrology and Earth System Sciences**, v. 6, n. 1, p. 85-100, 2002.

AVARES, C.J.; RIBEIRO JUNIOR, W.Q.; RAMOS, M.L.G.; PEREIRA, L.F.; CASARI, R.A.C.N.; *et al.* Water stress alters morphophysiological, grain quality and vegetation indices of soybean cultivars. **Plants**, v. 11, n. 4, p. 559, 2022. doi

TIAN, J.Y.; WANG, L.; LI, X.J.; GONG, H.L.; SHI, C.; *et al.* Comparison of UAV and WorldView-2 imagery for mapping leaf area index of mangrove forest. **International Journal of Applied Earth Observation and Geoinformation**, v. 61, p. 22-31, 2017. doi

THORP, K.R.; TIAN, L.F. A review on remote sensing of weeds in agriculture. **Precision Agriculture**, v. 5, n. 5, p. 477-508, 2004.

TUCCI, C.E.M. **Hidrologia: Ciência e Aplicação. 4ª edição**. ed. Porto Alegre: Editora da UFRGS, v. 4, 2012.

USAMENTIAGA, R.; VENEGAS, P.; GUEREDIAGA, J.; VEGA, L.; MOLLEDA, J.; BULNES, F.G. Infrared thermography for temperature measurement and non-destructive testing. **Sensors**, v. 14, n. 7, p. 12305-12348, 2014. doi

VADEZ, V.; KHOLOVA, J.; MEDINA, S.; KAKKERA, A.; ANDERBERG, H. Transpiration efficiency: new insights into an old story. **Journal of Experimental Botany**, v. 65, n. 21, p. 6141-6153, 2014. doi

VALE, B.S.; ROIG, H.L.; NEUMANN, M.R.B.; FERNANDES, E.S.; SALLES, L.A.; *et al.* Desempenho dos modelos SEBAL e SSEBop na estimativa da evapotranspiração do trigo no Cerrado. **Revista Brasileira de Meteorologia**, v. 37, p. 329-345, 2022. doi

WESTOBY, M.J.; BRASINGTON, J.; GLASSER, N.F.; HAMBREY, M.J.; REYNOLDS, J.M. Structure-from-Motion'-photogrammetry: A low-cost, effective tool for geoscience applications. **Geomorphology**, v. 179, p. 300-314, 2012.

ZHU, X.; LIU, D. Improving forest aboveground biomass estimation using seasonal Landsat NDVI time-series. **ISPRS Journal of Photogrammetry and Remote Sensing**, v. 102, p. 222-231, 2015.